Catalysis
Science &
Technology

Accepted Manuscript

ROYAL SOCIETY
OF CHEMISTRY

www.rsc.org/catalysis

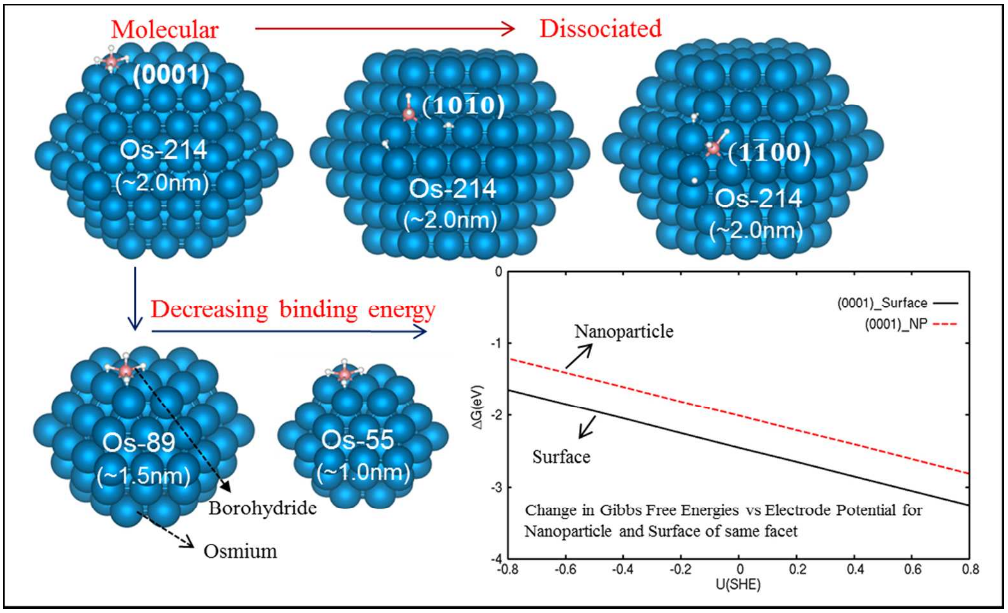

The first DFT study of borohydride interaction with Os nanoparticle/surfaces, clarifying effects of facets, size and local sites is presented.
183x110mm (150 x 150 DPI)

First-principles study of borohydride adsorption properties on Osmium nanoparticles and surfaces: understanding facet, size effects and local sites

Mary Clare Sison Escaño[a†], Ryan Lacdao Arevalo[b*], Elődd Gyenge[d] , Hideaki Kasai[b,c]

[a]Graduate School of Engineering, University of Fukui, 3-9-1 Bunkyo, Fukui, Japan, 910-8507

[b]Department of Applied Physics, Osaka University, 2-1 Yamada-oka, Suita, Japan, 565-0871

[c]Center for Atomic and Molecular Technologies, Osaka University, 2-1 Yamadaoka, Suita, Osaka 565-0871, Japan

[d]Department of Chemical and Biological Engineering and Clean Energy Research Centre, The University of British Columbia, Vancouver, BC V6T 1Z3, Canada

We present the first density functional theory investigation on the adsorption properties of borohydride between Os surfaces and nanoparticles with respect to facets, size and local sites. We found that the adsorption configuration and the binding energy significantly change with respect to these factors. On Os surfaces, the most stable adsorbate configuration is molecular on (0001) but dissociated on $(10\bar{1}0)$ and $(1\bar{1}00)$. For the Os nanoparticles, the preferred configurations on the Os surface are preserved only on the counterpart (0001) and $(10\bar{1}0)$ planes and the binding energies are significantly larger due to the presence of vertices/edges. The differing structures between the $(1\bar{1}00)$ facet of the slab and the nanoparticle is attributed to much different Os lateral distance. With respect to the nanoparticle size, the adsorbate structure is also preserved but the binding energy increases when the particle size is increased. At various electrode potentials, the borohydride oxidative adsorption is less favorable on the ~2.0nm Os nanoparticle as compared to the Os surface of the same facet due to an enhanced solvation at the vertex sites of the former. Finally, using *ab-initio* molecular dynamics, we found that these less coordinated sites of the Os nanoparticle reconstruct significantly with temperature especially for smaller sized ones. Only when the nanoparticle size is ~2.0nm that these reconstructions become minimal. These findings pose fundamental borohydride adsorption information on nanoparticle and surface facets relevant for modeling/screening of suitable nanostructures of anode catalysts for direct borohydride fuel cell.

Keywords: borohydride, adsorption, metal nanoparticle, metal surfaces, osmium, direct borohydride fuel cells, density functional theory.

[†] Corresponding author: mcescano@u-fukui.ac.jp
[*] on leave from the Philippine Normal University, Manila 1000, Philippines

1. Introduction

There has been a growing demand for power sources for myriad of applications ranging from portable devices to large scale stationary power. In the area of portable power sources, micro-fuel cells such as the direct methanol fuel cell with simple cell design, are attractive alternatives to batteries due to high theoretical gravimetric energy density, which offers the possibility of extended operating time and shorter refueling time compared to the typical full recharge times of batteries. However, carbonaceous fuels utilized in micro fuel cells face severe performance limiting issues related to the necessity of using Pt-based catalysts, that in addition to being expensive, could suffer from carbon monoxide (CO) poisoning, compromising the durability [1,2]. The direct borohydride fuel cell (DBFC) offers significant advantage compared to methanol and other carbonaceous fuels. Some of these advantages are: higher theoretical gravimetric energy density (i.e. 9.3 Wh/g vs. 5.9 Wh/g for methanol), inherent absence of CO poisoning of the anode catalyst, enhancing both the power output and durability and offering the possibility of using non-platinum anode and cathode catalysts in alkaline media [3]. Regarding the discovery of non-Pt based anode catalysts for DBFC, it was shown that Os can act as efficient electro-oxidation catalysts for BH_4^- [3-6]. Using amorphous Os thin-film electrode suitable for microfluidic devices, a maximum Os catalyst mass-specific activity of about 1240 A g^{-1} is reported [5]. Also, the effectiveness of Os nanostructured extended reaction zone anodes in the “Swiss-roll” mixed reactant DBFC has been demonstrated [6].

From a catalytic point of view, borohydride is competitively involved in two reactions types on the anode. One is the direct electro-oxidation with a theoretical maximum number of electrons exchanged equal to eight:

$$BH_4^- + 8OH^- \rightarrow BO_2^- + 6H_2O + 8e^- \quad E^{\circ}{}_{298K} = -1.24\,V\ vs.SHE \qquad (1)$$

and the other reaction is thermo-catalytic hydrolysis (or decomposition):

$$BH_4^- + 4H_2O \rightarrow B(OH)_4^- + 4H_2 \quad (2).$$

The competition between reactions (1) and (2) coupled with possible H_2 oxidation, will determine the overall faradaic efficiency of the anode. The ideal catalytic scenario would be to completely suppress reaction (2). Most of the anode catalysts that are active for reaction (1) such as Pt and Pd are also active for reaction (2) [7-9]. However, Os catalyst has been demonstrated to be virtually inactive toward reaction (2) [6]. Hence, coupled with the high activity for reaction (1) as mentioned previously, Os is a promising catalyst for borohydride oxidation.

From theoretical point of view, the BH_4^- oxidation has been studied by only a few groups on selected transition metal model surfaces among them Pt (111) and Au (111) being the most investigated cases [10-13]. Briefly, the selectivity is governed by the configuration of surface bound borohydride denoted by $BH_y^* + (4-y)H^*$, generated from initial oxidative adsorption:

$$BH_4^- + *\,(metal\ site) \rightarrow BH_y^* + (4-y)H^* + e^- \quad (3),$$

where $y = 1, 2$ or 3, leading to dissociated structures (e.g. BH^* + $3H^*$, BH_2^* + $2H^*$, BH_3^* + H^*) or alternatively, $y = 4$, resulting to a molecular structure (BH_4^*) {(*) indicates an adsorbed specie}. On fcc (111) slab of Pt, the strong adsorption and the easily generated dissociated structure of borohydride, BH^* + $3H^*$ support the metal's tendency to catalyze reaction (2) and also the direct oxidation (1) but with less than 8 electrons exchanged. Hydrogen evolution has been evident in this system [7-9]. On the other hand, Au(111) interaction with borohydride leads to a molecularly adsorbed specie, BH_4^*, which suggest preference for direct oxidation (1) [10,12-14]. Such initial molecular borohydride adsorption correlation with complete oxidation and suppression of hydrogen evolution has been confirmed by surface enhanced Raman spectroscopy (SERS) in combination with density functional theory (DFT) [15]. Nevertheless, the interaction of Au with borohydride is much weaker as compared with other transition metals, and therefore higher anodic overpotential has been experimentally observed [16-18].

In order to understand the borohydride-metal interaction in line with the more commonly used catalysts morphologies such as nanoparticles (NP), a departure from the typical (111) faceted metal slabs should be considered. Thus, the goal of the present work is to investigate the borohydride adsorption properties such as geometry and binding energies as a function of different facets of metal slabs/surfaces and different planes of NPs. Furthermore, comparisons between the interaction of borohydride with the metal surface and with the NP are made to analyze the effect of the local adsorption sites. The role of NP size on the adsorption is also discussed. At present, this fundamental information correlating adsorption of borohydride with the nature of the catalyst surface is not available. To the best of our knowledge, there has been no information on the adsorption of borohydride on a nanoparticle. The evaluation of the adsorption properties is implemented on Os due to the aforementioned experimentally observed beneficial electrocatalytic effect [3-6]. More importantly, although Os is a platinum group metal (PGM), it is 4-5 times cheaper than Pt , therefore, in addition to its experimentally observed effectiveness, Os could serve as a model for an ideal anode catalyst. These facts triggered our interest in gaining valuable insights into the adsorption properties of borohydride on Os surfaces and nanoparticles.

2. Computational Methods

The theoretical work conducted to study the adsorption properties of borohydride molecule on different Os metal surface facets and Os NP planes is based on density functional theory (DFT) [19,20], which is implemented in Vienna Ab-initio Simulation Package (VASP) [21-24]. The exchange-correlation functional is described by generalized gradient approximation (GGA) of Perdew, Burke and Ernzerhof (PBE) [25] and the ion-valence electrons interaction is modeled using projector augmented wave method (PAW) method [26,27]. Plane-wave expansions are conducted with kinetic energy cut-off of 400eV. These calculation parameters lead to the hcp Os bulk lattice constant, a of 2.750Å and the c/a ratio of 1.580 (c is the axis normal to plane of a) in excellent agreement with experiment, a=2.740Å and c/a = 1.579 [28]. These bulk parameters are used for all the initial dimensions of metal slabs and NPs. For the Os surfaces, supercells with slabs of four and eight layers corresponding to the basal (Os (0001)) and prism planes (Os $(10\bar{1}0)$ and $(1\bar{1}00)$), respectively, are used based on the convergence of surface energies. The vacuum thickness in all supercells is ~14.0Å and the surface unit cell size is (1x1). The surface unit cell is expanded to (3x3) for the adsorption calculations. In the slab optimization, the conjugate gradient minimization method [29] is used and the iterations are terminated when the Hellman-Feynman forces on each atom is converged to 0.01eV/Å^3. The Brillouin zone integration is performed on a grid of (4x4x1) Monkhorst-Pack *k* points and a smearing of Methfessel-Paxton method [30]. The optimized Os (0001), $(10\bar{1}0)$ and $(1\bar{1}00)$ surfaces are shown in Figure 1a, 1b and 1c, respectively. Briefly, we note that in Figure 1a, the first interlayer distance, d_{1-2} of 2.71Å gives a 3.23% inward surface relaxation, in agreement with other DFT calculation, 3.79% [31]. In Figure 1b and 1c, the $(10\bar{1}0)$ and $(1\bar{1}00)$ surfaces show presence of shallow trenches which lead to a much smaller d_{1-2}. The parallel rows on these facets result to a lateral distance, *b* and a top - subsurface atom separation distance, ***c***. Details of the calculations for the adsorption of borohydride on these three facets are discussed in the later section.

For the nanoparticle cases, regular polyhedral structures such as cuboctahedral, icosahedral, octahedral and hexagonal closed packed or HCP are the most commonly used models for 5d transition metals [32-35]. Due to the hcp structure of Os, the hexagonal closed packed (HCP) is considered. Moreover, because of the higher probability and stability of closed shell structures with the magic number of atoms, then the Os NP with magic numbers: 57, 89 and 214 corresponding to a diameter of ~1.0nm, ~1.5nm, ~2.0nm are chosen. Using these numbers to represent the sizes, the nanoparticles are then labeled as Os-57, Os-89 and Os-214. The NPs are optimized using supercells with very large vacuum of ~25Å , which separates the nanoparticle from its periodic image in all directions. The Γ-point is appropriate for the Brillouin zone integration. The same exchange-correlation functional, method of description of ion-valence electrons interaction, algorithm for optimization and kinetic energy for plane wave expansion employed in the surface calculations are used for the nanoparticle calculations as well. The details of the optimized geometries of the NPs are given in Table 1, and the resulting structures are shown in Figure 2. In Table 1, we note that the cohesive energies (E_c) increase as the NP size increases. E_c is calculated using the following expression:

$$E_C = nE_a - E_T \qquad (4),$$

where E_T is the total energy of the cluster, E_a is the total energy of isolated Os atom and n is the number of Os atoms in the cluster. We expect the E_c to tend towards the bulk value for much larger NPs. For the geometry, the α_{NP} gives the Os-Os bond distance (see Figure 2). Also, we note that the α_{NP} increases as the nanoparticle size increases. Further, in Table 1, $\boldsymbol{n}$ and M pertain to the number of shells in the NP and the magnetic moment per atom respectively. It can be noted that there is no spin moment for all NP sizes and thus, they retain the same non-magnetic property of the Os bulk and metal surface. When it comes to 4d and 5d transition metal clusters, the onset of magnetic ordering arises in the quantum size region where the clusters are sufficiently small, which is understandable based on the concept of discontinuity in the electronic spectrum as the cluster size decreases. The same concept leads to a significant spin-orbit (SO) coupling effect for such cluster sizes. Hence, the non-magnetic property exhibited even by the smallest Os cluster size of 1.0nm considered in this work , indicates that SO is still minimal (NPs are large enough that electron states are still well dispersed) and is therefore not influential in the assessment of the ground state properties. Furthermore, Figure 2 shows that apart from the prominent (0001) plane of HCP structure, the $(10\bar{1}0)$ and $(1\bar{1}00)$ planes also arise at the sides. Some atoms belonging to these planes are marked by the dashed lines. The computational details for the adsorption on these

NP planes will be discussed in the later sections. Next, the initial oxidative adsorption of borohydride on the metal slab and the NP, which takes into account solvation and electrode potentials are compared. The scheme based on the vacuum-slab method [36,37] is devised to suitably conduct the comparative studies. This scheme will also be detailed towards the end of the next section. Lastly, since temperature effects can change the geometry of NP in a much significant fashion than on metal surfaces, therefore, we performed simulated annealing via *ab-initio* molecular dynamics (MD) to determine the extent of the changes in the geometry of Os NP with respect to size and thus be able to draw implications of temperature on adsorption. Here, the systems are equilibrated at high temperature of 1100K and cooled to 300K. The equilibration is conducted using microcanonical MD with timestep of 2 fs and MD steps of 2000. For the electronic minimization, the residual minimization method (RMM-DIIS) [38,39] is used. The relaxation of the electronic degrees of freedom is terminated if 10^{-4} energy change is reached. The details of the evaluation of the changes in the geometry of Os NP and their implication on adsorption properties are also discussed in the latter sections.

3. Results and Discussions

3.1 Adsorption on Os metal surfaces

The search for the preferred adsorption configuration of borohydride on Os metal surfaces is performed by potential energy scanning (PES). Figure 3a illustrates the PES conducted for (0001) facet and the inset figure shows the isolated trigonal borohydride molecule. The calculated B-H bond distance of the isolated state is 1.25Å and the H-B-H angle is 109° in excellent agreement with experiment [40]. To execute the PES, the center-of-mass (c.m) of this molecule (which is boron, B) is placed on different high symmetric sites: bridge (*b*), hollow (*h1, h2*) and top (*t*) with the three B-H bonds oriented downwards as shown in Figure 3a. Configurations where the three H's point away from the surface (i.e. inverted configuration) are not stable [10-14], thus they are not considered in this work. Then, an in-plane rotation of the molecule is conducted to explore the potential minimum. We conveniently named the initial configurations using the position of the c.m. and the direction by which most of the B-H bonds span. For instance, *b-b*, indicates that the B is on the bridge site and the B-H bonds span towards the bridge site as well. Table 2 lists all the initial configurations considered for (0001) facet. The adsorption energy of the molecule is obtained using the following:

$$E_b = E_T - (E_{slab} + E_a) \qquad (5),$$

where E_T is the total energy of the adsorbed system, E_{slab} is the total energy of the bare slab and E_a is the total energy of the molecule in gas phase. Table 2 gives the values for E_b, the corresponding final structures and the final B-H distances. First, we focus on the generated specie/s, $BH_y^* + (4-y)H^*$ as described previously in reaction (3). We note that the most stable final configuration on (0001) facet is molecular, BH_4^* with a binding energy of -4.96eV (Table 2, bold form). This originated from the same initial *h1-t* configuration (Figure 3b). The optimum B-H bond lengths near the surface, denoted as B-H2,3,4 in Table 2 are 1.44-1.45Å. This is longer as compared to the isolated borohydride. Other relevant Os-Os distances and bond lengths as a consequence of the binding of the molecule with the (0001) facet are shown in Figure 3b. Both the interlayer distances, $d_{1\text{-}2}$ (at the binding sites) and $d'_{1\text{-}2}$ (near the binding sites) are not significantly affected. The effect of the adsorption on the metal is more of a lateral expansion (**a**, and **a'**) with very little change on vertical distances. The next stable structure belongs to the *b-t* initial configuration (Table 2, italized). This final structure turns out to be a borohydride with one dissociated B-H bond, $BH_3^* + H^*$. Because of the proximity of the binding energy of this structure to that of the *h1-t*, then using the climbing nudged elastic band method [41,42], we calculated the activation barrier for H abstraction from BH_4^* and obtained a value of 0.30eV. This is large enough to keep the BH_4^* in the *h1-t* configuration as the most stable on Os (0001). Finally, the B-H1 bond lengths (H1 is the hydrogen that points out of the surface) for all final structures are very similar, 1.19-1.22, but are smaller than that of the isolated molecule.

With respect to the adsorption on other facets of the Os metal slab, the same optimization scheme is implemented. The high symmetric sites on $(10\bar{1}0)$ and $(1\bar{1}00)$ surfaces are shown in Figure 4a and Figure 5a, respectively. On $(10\bar{1}0)$, five initial c.m. can be identified: bridge between the atoms along the rows (*b1*) and in between the rows (*b2*), fourfold hollow (*h1*), three-fold hollow (*h2*) and the top (*t*) sites. The *h2* site is at the center of the three atoms that form the vertices of the triangle indicated by dashed lines in Figure 4a. One of these atoms belongs to the subsurface. Table 3 lists nine initial configurations. The most preferred geometry arises from the *b2-t* with a binding energy of -5.64eV (Table 3, bold form). This is larger than that of (0001) facet. Interestingly, this most stable final structure is a partially dissociated borohydride, BH_2* + 2H* as depicted in Figure 4b. The BH_2* is situated at the *b2* site and the dissociated 2H* are on *b1* sites. The B-H bond length in BH_2* is 1.42Å and the 2H* distance from B is 2.99Å (Table 3). In contrast to the adsorbate effect on the Os (0001), significant changes can be noted for the interlayer spacings at the binding site, $d_{1\text{-}2}$, $d_{2\text{-}3}$ and near the binding sites, $d_{1\text{-}2'}$ and $d_{2\text{-}3'}$. The presence of both lateral (**a**,**b**,**c**) and vertical reconstructions ($d_{1\text{-}2}$, $d_{2\text{-}3}$) are due to the more open structure of $(10\bar{1}0)$ surface. Furthermore, the presence of the shallow trenches also allows for the interaction of the molecule with the subsurface atoms. Here, the B atom conforms with three Os atoms (indicated by the triangle in Figure 4b), two of which belong to the subsurface. Lastly, all the B-H1 bond lengths of the final structures are within the range of 1.20-1.21 Å, similar with that of (0001) facet.

For the Os$(1\bar{1}00)$, out of four possible sites for the c.m as shown in Figure 5a and in-plane rotations of the molecule, eight initial adsorption configurations can be derived. It is found that the most stable geometry originates from the initial *h-b1* configuration with binding energy of -6.72eV (Table 4, bold form). Note that this is much larger than the binding energy of the most stable species on the previous two facets. The final structure is an almost fully dissociated BH* + 3H*, where the B-H distances are within the range of 3.31-3.35Å - also the longest among the three facets. Figure 5b depicts the binding sites and the changes in the Os surface structure. First, the BH* is situated at the hollow site formed from two row atoms and two “trench” atoms (depicted by the square in Figure 5b), while the 3H* are all in the *b1* sites. Thus, conformation of B with subsurface atoms as in $(10\bar{1}0)$ is noted. Furthermore, similar reconstructions as that of $(10\bar{1}0)$ are observed, also owing to the open structure of $(1\bar{1}00)$ facet. The largest value of B-H1 bond length across all facets is found only on $(1\bar{1}00)$ via the *h-b1* configuration (~1.23Å). This is due to the bent structure of the BH* making the H1 closer to the surface.

The stable structures of borohydride generated out of its oxidative adsorption described by the expression (3) has been theoretically explored on various fcc(111) surfaces of 4d, 5d transition metals such as Pt and Au [10-14]. The stable adsorbate structures in this group have been either molecular, BH_4* (Au) or almost fully dissociated BH* + 3H* structures (Pt). In comparison with Os (0001), the same molecular structure as that of Au(111) is noted but with a greater binding energy (in fact, close to that of Pt(111)), making Os attractive for suppression of H_2 evolution and at the same time for less overpotential due to stronger molecule-Os interaction than Au. Further, in the present work, by using other Os facet such as $(10\bar{1}0)$, for the first time, a different geometry within the platinum-group metal is identified - BH_2* + 2H*. So far, such an adsorbate structure has been proposed only for 3d fcc(111) Mn and Fe, which have been so far considered as alloying components [11,14,43]. Finally, the easy tendency towards breaking a B-H bond in the more open facets of Os as compared to

(0001), can be drawn based on Bronsted-Evans-Polanyi (BEP) relation and from the molecule-surface interaction. The adsorption energy of the most stable configurations increases in the order (0001)< $(10\bar{1}0)$< $(1\bar{1}00)$ and so the activation energy is expected to decrease in the same order: (0001)> $(10\bar{1}0)$>$(1\bar{1}00)$.

3.2 Adsorption on Os NP

We begin with the discussion of the adsorption of borohydride on the different planes of NP. We consider the Os-214 as it gives an NP model that can strike a balance between computational cost and adequacy of the NP size (~2.0nm). Os-214 is also not prone to significant geometry changes due to temperature as compared to the smaller sized ones, as we will further discuss later. Figure 6a-h shows the eight initial adsorption configurations (depicted by the triangles) and final optimized structures (depicted by the atoms). In the representation of the initial sites, vertices of the triangles represent the trigonal conformation of the H atoms with the plane of NP and the center of the triangles describes the position of the B atom. First on the (0001) plane, Figure 6a, b and c show an *h1-t* configuration at the center (no conformation with edge atoms), at the edge-vertex combination site (participation of one edge atom and one vertex atom) and at the edge site (participation of two edge atoms), respectively. So, this evaluates the role of the number of low coordinated sites on NP. The adsorption energy, E_{b-NP}, is obtained using the following expression:

$$E_{b-NP} = E_T - (E_{NP} + E_a) \quad (6),$$

where E_T is the total energy of the adsorbed system and E_{NP} is the total energy of the bare NP. Table 5 shows the initial configuration, which are labeled as (a)-(h) and summarizes the adsorption properties. We found that, the **(b)** initial configuration gives the most stable adsorption (Table 5, italized). The final structure is molecular, BH_4*, with binding energy of -5.33eV. The **(c)** initial configuration gives the next stable adsorption and the final structure is also molecular with binding energy of -5.15eV. Lastly, the **(a)** initial configuration, gives the least stable adsorption which is also molecular (-5.05eV). The **(b)** > **(c)** > **(a)** order of the adsorption energies clarifies the role of the number of the vertex and edge atoms involved in the conformation with the molecule. The greater is this number, the stronger is the adsorption energy. Next, in comparison with the (0001) facet of the metal slab, the adsorption strengths on the (0001) plane of NP are much greater due to these local sites. Such trend between the adsorption on slab versus nanoparticle has been observed experimentally for oxygen on

Pd using direct calorimetric measurements in combination with temperature-programmed desorption [44].

For the $(10\bar{1}0)$ plane, Figure 6d and f show the initial conformation via bridge sites and Figure 6e shows the *h1-t* initial adsorption structure. The most stable adsorption arises from the **(d)** initial structure, with a binding energy of -5.71eV (Table 5, bold form). Here, the final structure is a partially dissociated borohydride, $BH_2^* + 2H^*$, whose B-H bond length in BH_2^* is ~1.43 Å and the dissociated B-H distances are between 2.85-3.09Å. This is also the most stable structure across all the planes of Os-NP. In comparison with $(10\bar{1}0)$ facet of Os surface, the same most stable partial dissociated structure has been found (recall Figure 6). The B-H distances are also similar (Table 3) but the binding energy on the slab is smaller (-5.64eV).

For the $(1\bar{1}00)$ plane, Figure 6g and h show the initial bridge and hollow site adsorption, respectively. The most stable adsorption belongs to the initial **(h)** configuration which optimizes into a $BH_2^* + 2H^*$ structure with adsorption energy of -5.61eV (Table 5, underscored). In comparison with $(1\bar{1}00)$ facet of Os slab, this structure is different. The most stable configuration on the Os surface is $BH^* + 3H^*$. Furthermore, the adsorption energy on the NP is smaller compared to the metal slab (-6.72eV as given in Table 4) contrary to the previous two facets. We note that this difference in the final adsorbate structures between the slab and the NP is due to the unbroken B-H bond of the BH_2* on the latter. From Table 5, we note that this bond is already stretched to 1.59Å – the longest among all the molecular bond lengths identified on NP. However, the H separation from B atom is restricted by the larger distance between the boron and the next neighboring bridge site where H can settle most favorably (marked by X in Figure 6). In fact on NP, two hydrogen sit instead on the top sites giving the less stable final BH_2* + 2H* structure. Thus, the accessibility of the favorable hydrogen adsorption site contributes to the difference in geometry of the adsorbate between the slab and the NP. Over-all, the BH* + 3H* structure is in fact very common and the most stable configuration on fcc(111) facet of 5d transition metal slabs such as Pt, Pd [10,12]. However, on the Os-NP, we note that this final structure is not prevalent, confirming the less susceptibility of Os catalysts towards reaction (2) as observed in experiments [3-6].

Lastly, we evaluate the effect of NP size on the adsorption. Using the (0001) plane, which was found to produce a desirable molecular form of borohydride, the final structures and the corresponding binding energies across all NP sizes considered in this work are determined. The molecule assumes the same initial *h1-t* configuration as was used on the Os-214. Table 6 details the adsorption properties and Figure 7 shows the corresponding adsorption structures. We note that the final structure on all NP sizes is molecular, BH_4*. However, the range of the B-H bond lengths is wider for bigger NP size. Moreover, the adsorption energy from the smallest NP increases in the order: Os-57 (-4.79eV) < Os-89 (-4.85eV) < Os-214 (-5.33eV). This is basically due to the increasing Os-Os distance (a_{NP}) as the NP size is increased. Larger interatomic distances suggest less overlap of the d-states of the metal and therefore a higher entire d-band and a more enhanced reactivity.

3.3 Initial oxidative adsorption between Os surface and Os-NP

In this section, we investigate the initial oxidative adsorption described in reaction equation (3) on Os metal slab and on Os-NP at various electrode potentials. Previously, we focused on the details of the adsorption properties such as structures of the species generated out of this initial oxidative adsorption which, as described previously, is of prime importance as to the tendency of the catalyst preference for reaction (1) or (2). Here, we investigate the favorability of the initial oxidative adsorption itself on Os slab and on NP to derive factor(s) significant in the oxidative process between these two morphologies. This process would involve treatment of the solvation of the species and the surface, electrode potential and the Gibbs free energies of adsorbed species. As mentioned previously, the vacuum slab model is used to conduct the comparative study, where the Os (0001) slab and the (0001) plane of Os-214 are considered due to the desirable adsorbate structure and the relatively simple reconstructions on this facet. Using reaction (3) and the final adsorption configuration of the generated specie associated with (0001) plane, the reaction can be rewritten as:

$$BH_4^- + * \,(metal\ site) \rightarrow \boldsymbol{BH_4^*} + e^- \quad (7)\,,$$

where e^- is the electron charge transferred to the electrode. By taking into account a solution phase, we can modify this reaction by allowing solvation of the ion, $BH_4^-{}_{aq}$ and the surface by water molecule substitution upon oxidative adsorption as given in the following:

$$BH_4^-{}_{aq} + H_2O^* \rightarrow BH_4^* + H_2O_{aq} + e^- \quad (8)\,.$$

Thus the change in Gibbs free energy for this reaction can be described as:

$$\Delta G_{ads} = G_{BH_4^*} + G_{H_2O_{aq}} - G_{BH_4^-{}_{aq}} - G_{H_2O^*} - eU \quad (9)\,,$$

where U is the electrode potential on the vacuum scale. If referenced to SHE, then:

$$\mathrm{U}_{SHE} = \mathrm{U} - 4.46\mathrm{V} \quad (10)\ .$$

The free energy of the adsorbed species, G_{A^*} (where $A^* = BH_4^*,\ H_2O^*$) is the ground state energy, E_{DFT} adjusted by adding zero-point vibrational energy (E_{ZPVE}) and vibrational entropy $(S_{vib}T)$ terms:

$$G_{A^*} = \mathrm{E}_{DFT} + E_{ZPVE} - S_{vib}T \quad (11)\ ,$$

where $\mathrm{T} = 298\mathrm{K}$ and the E_{ZPVE} and $S_{vib}T$ are described as:

$$E_{ZPVE} = \frac{1}{2}\sum_i hv_i \quad (12)\ ,$$

$$S_{vib}T = k_BT\sum_i \left\{\frac{hv_i}{k_BT}\left[exp\left(\frac{hv_i}{k_BT}\right) - 1\right]^{-1} - ln\left[1 - exp\left(-\frac{hv_i}{k_BT}\right)\right]\right\} \quad (13)\ .$$

The modes of vibrational frequency (v_i) are obtained by finite difference dynamical matrix (step size is 0.015Å) [45,46] and the h, k_B are Planck's constant and Boltzmann constant, respectively. For reference, the values of the parameters as discussed above are summarized in Table 7. Next, the free energy of the solvated species, A_{aq} (i.e. $\mathrm{BH}_{4\,aq}^-$, H_2O_{aq}), is obtained by the inclusion of solvation, ΔG_{sol} as taken from literature [47,48] and a correction term for concentration to the gas phase free energy, G_A :

$$G_{A_{aq}} = \quad G_A \quad + \Delta G_{sol} + k_B T ln[A] \quad (14) .$$

The plot of the $\Delta \mathrm{G}_{ads}$ obtained from equation (9) at various electrode potentials, $\mathrm{U_{SHE}}$ for (0001) plane of the slab and the Os-NP is shown in Figure 8. We note that the oxidative adsorption of borohydride is favorable ($\Delta \mathrm{G}_{ads} < 0$) at all potentials of interest. However the adsorption is more preferred (more negative $\Delta \mathrm{G}_{ads}$) on the metal slab than on the Os-NP. Generally, on metal surfaces, the greater is the binding energy of the surface bound species, the more favorable is the initial oxidative adsorption [13,14]. In this case, however, the binding energy of BH_4^* on (0001) surface is weaker (-4.96eV from Table 2) as compared to that of the (0001) plane of Os-NP (-5.33eV (from Table 6). We note that the lower $\Delta \mathrm{G}_{ads}$ on the Os-NP is attributed to its greater tendency for solvation. On NP, water molecule is much more bound (-1.53eV at vertex site) than on metal surface (-0.73eV) leading to higher energy cost for water substitution upon borohydride adsorption as described in reaction (8), and thus lowering the ΔG_{ads} as defined in equation (9).

3.4 Os-NP at 300K

Due to the major role played by the presence of the edge/vertex atoms on the Os-NP on borohydride adsorption suggests another (external) factor that can possibly alter NP reactivity such as temperature. As observed previously, adsorbate configurations arising from the conformation of the molecule at edges/corners of the NP are often the most stable. Furthermore, we have noted above the effect of these sites on solvation of NP, which in turn affect oxidative adsorption process. These local sites are more unstable as compared to surface atoms and are therefore more vulnerable to temperature effects. Therefore, in this work, we investigated the geometric changes on such local structures with respect to increase in temperature on all the Os-NPs using *ab-initio* MD. As described in the computational methods section, the NPs are annealed to 1100K, cooled down to 300K. At this lower temperature, the final structure is obtained and the local sites are evaluated. The changes in the geometry (or reconstruction) are grouped into: (1) a_{ave}, which pertains to the average lateral distance involving one vertex and one edge atom of (0001) plane; (2) b_{ave}, which is the lateral distance involving one vertex and one edge atom at $(10\bar{1}0)$ plane; and (3) the $\angle c_{ave}$, which is the angle between the Os-Os bonds at the edge of $(1\bar{1}00)$ plane. These are all depicted in Figure 9. The a_{ave}, b_{ave} and $\angle c_{ave}$ values per NP size are detailed in Table 8. As for the reference, we used the a_{ave}, b_{ave} and $\angle c_{ave}$ of the DFT-optimized NPs at 0K, which are shown inside the parentheses. First, we note that there is minimal change in the a_{ave}. The b_{ave} however is significantly elongated especially for the smaller NP sizes (Os-57 and Os-89). For the $\angle c_{ave}$, Os-57 and Os-89 have smaller values, indicating significant buckling of $(1\bar{1}00)$ plane on these sizes. The above observations indicates that the (0001) plane of NP is not affected by temperature as much as the other two planes. Also, more importantly, the results indicate that only the NP of size ~2.0nm and beyond have minimal changes in the geometry of the planes. In terms of the implications of the reconstructions on adsorption of borohydride, first, the elongation of the b_{ave} due to temperature prominently observed for smaller sized NPs suggests stronger adsorption. The buckled $\angle c_{ave}$ also especially for small NPs leads to enhanced protrusion of vertex sites making these locations more reactive. Furthermore, this buckling decreases the separation of next neighboring bridge sites and thus may promote B-H bond dissociation. The confirmation of these implications on the borohydride oxidation on annealed Os catalysts both theoretically and experimentally is worthwhile.

4. Conclusions

First-principles calculations based on density functional theory are conducted to investigate the role of facet in the adsorption of borohydride on Os metal surfaces and on nanoparticles. We found that the most stable adsorption configuration on the Os surfaces differs for each facet: molecular (BH_4^*) on Os(0001), partially dissociated (BH_2* + 2H*) on Os $(10\bar{1}0)$ and an almost fully dissociated (BH* + 3H*) structure on Os $(1\bar{1}00)$. The binding energies are also different: -4.96eV (0001) < -5.64eV $(10\bar{1}0)$ < -6.72eV $(1\bar{1}00)$. In the case of Os-NP, we found that the configuration of the stable specie also differs with respect to the NP planes. The stable final structure is molecular (BH_4^*) on (0001), partially dissociated (BH_2* + 2H*) on $(10\bar{1}0)$, and also partially dissociated (BH_2* + 2H*) on the $(1\bar{1}00)$ plane. The binding energies increase in the following order: -5.33eV (0001) < -5.61eV $(1\bar{1}00)$ < -5.71eV $(10\bar{1}0)$. Comparison of these adsorption properties between the Os surface and NP, indicates that the final structure is similar for (0001) and $(10\bar{1}0)$ facets but the binding energies are larger on the NP. These differences between the slab and the NP point to the more complex geometry of the latter. We note that due to the presence of the edge/vertex atoms, which have less coordination as compared to the atoms on the surfaces, the adsorption on the NP are stronger. For the $(1\bar{1}00)$ facet, the final adsorbate structures are different due to the unbroken B-H bond of the BH_2* on the NP. The restricted H separation from B atom is inhibited by the larger distance between the boron site and the next neighboring bridge site (where H adsorption is favorable) as compared to that of the Os $(1\bar{1}00)$ slab. In terms of the initial oxidative adsorption as a function of electrode potential, also the "local" structures serve as the origin of the differences between the Os surface and Os-NP, where the latter can promote solvation at the surface. We found that water is strongly bound at the edge/vertex sites of NP, making oxidative adsorption of borohydride less favorable due to higher energy cost to dislodge water molecule for borohydride adsorption. The local structures on NP, which play vital role in the final structures of the adsorbates as well as on the oxidative adsorption of borohydride, are found to easily reconstruct on the more open $(10\bar{1}0)$ and $(10\bar{1}0)$ planes with temperature. Furthermore, we found that such instability is more profound on small nanoparticles. It is observed that only from Os-214 of size ~2.0nm that these reconstructions can be minimized. These finding pose significant insights on suitable nanostructures for both modeling and synthesis of DBFC anode catalysts.

Acknowledgments

M.C.S. Escaño extends gratitude to Tenure Track Program for Innovative Research, Ministry of Education, Culture, Sports, Science and Technology, Japan (MEXT) and Japan Science and Technology Agency (JST) for research funds. Some of the calculations are done using Kyoto University Supercomputer and High-Performance Computing System (HPCS) of Escaño Research Group, University of Fukui. R.L. Arevalo extends gratitude to Ministry of Education, Culture, Sports, Science and Technology, Japan (MEXT) for scholarship.

References:

1. J. Ma, N.A. Choudhury and Y. Sahai, *Renew. Sust. Energ. Rev.* 2010, **14**, 183-199.

2. M. Jimenez, C.P. de León, A. A. Shah and F.C. Walsh, *J. Power Sources*, 2012, **219**, 339-357.

3. V. Lam and E. Gyenge, *J. Electrochem. Soc.* 2008, **155**, B1155-B2260.

4. V.W.S. Lam, D.C.W. Kannagara, A. Alfantazi and E. Gyenge, *J. Power Sources*, 2012, **212**, 57-65.

5. A. Ignaszak and E. Gyenge, *Electrochim. Acta* 2013, **95**, 268-274.

6. A. Aziznia, C.W. Oloman and E. Gyenge, *Chem. Sus. Chem.* 2013, 6, 847-55.

7. V.W.S. Lam, D.C.W. Kannangara, A. Alfantazi and E. Gyenge, *J. Phys. Chem. C* 2010, **115**, 2727-2737.

8. M. Simões, S. Baranton and C. Coutanceau, *J. Phys. Chem. C.* 2009, **113**, 13369-13376.

9. E. L. Gyenge, *Electrochim. Acta* 2004, **49**, 965-978.

10. G. Rostamikia and M. Janik, *Electrochim. Acta* 2010, **55**, 1175-1183.

11. R.L. Arevalo, M.C.S. Escaño, A.Y. Wang and Hideaki Kasai, *Dalton Trans.* 2013, **42**, 770-775.

12. M.C.S. Escaño, E. Gyenge, R.L. Arevalo and Hideaki Kasai, *J. Phys. Chem. C* 2011, **115**, 19883-19889.

13. R.L. Arevalo, M.C.S. Escaño and Hideaki Kasai, *J. Phys. Chem. C* 2012, **117**, 3818-3825.

14. R.L. Arevalo, M.C.S. Escaño and Hideaki Kasai, *ACS Catal.*, 2013, **3**, 3031-3040.

15. G. Rostamikia, A. J. Mendoza, M.A. Hickner and M. Janik, *J. Power Sources,* 2011, **196**, 9228-9237.

16. A. Ignaszak, D.C.W Kannagara, V.W.S. Lam and E.L. Gyenge, *J. Electrochem. Soc.* 2013, **160**, H47-H53.

17. M. Chatenet, M.B. Molina-Concha, J.P. Diard, *Electrochim. Acta* 2009, **54**, 1687-1693.

18. M.B. Molina-Concha and M. Chatenet, *Electrochim. Acta* 2009, 54, 6130-6139.

19. P. Hohenberg and W. Kohn, *Phys. Rev.* 1964, **136**, B864-B871.

20. W. Kohn and L.J. Sham, *Phys. Rev. 1*965, **140**, A1133-A1138.

21. G. Kresse and J. Furthmüller, *Comput. Mater. Sci.* 1996, **6**, 15-50.

22. G. Kresse and J. Furthmüller, *Phys. Rev. B* 1996, **54**, 1169-1186.

23. G. Kresse and J. Hafner, *Phys. Rev. B* 1993, **47**, 558-561.

24. G. Kresse and J. Hafner, *Phys. Rev. B* 1994, **49**, 14251-14269.

25. J. P. Perdew, K. Burke and M. Ernzerhof, *Phys. Rev. Lett.* 1996, **77** 3865-3868.

26. P. Blochl. *Phys. Rev. B* 1994, **50**, 17953-17979.

27. G. Kresse and J. Joubert. Phys Rev. B 1999, **59**, 1758-1775.

28. J.W. Arblaster, Platinum Metals Rev. 1989, **33**, 14-16.

29. M.P. Teter , M.C. Payne, and D.C. Allan, *Phys. Rev. B* 1989, **40**, 12255-12263.

30. M. Methfessel, A. Paxton, *Phys. Rev. B* 1989, **40**, 3616-3621.

31. V. Zólyomi, Kollár and L. Vitos, *Phys. Rev. B.* 2008, **78**, 195414(1) –(5).

32. A. H. Larsen, J. Kleis, K.S. Thygesen, J.K. Nørskov and K.W. Jacobsen, *Phys. Rev. B* 2011, **84**, 245429(1) –(13).

33. J.L.C. Fajín, A. Bruix, M. Natália, D.S. Cordeiro, J.R.B. Gomes and F. Illas, *J. Chem. Phys.* 2012, **137**, 034701-034711.

34. I.V. Yudanov, A. Genest, S. Schauermann, H.J. Freund and N. Rösch, *Nano Lett.* 2012, **12**, 2134-2139.

35. S.H. Noh, M. H. Seo, J. K. Seo, P. Fischer and B. Han, Nanoscale, 2013, **5**, 8625-8633.

36. A.B. Anderson, D.B. Kang, *J. Phys. Chem.*1998, **102**, 5993-5996.

37. J.K. Nørskov, J. Rossmeisl, A. Logadottir, L. Lindqvist, J.R. Kitchin, T. Bligaard and H. Jónsson, *J. Phys. Chem. B* 2004, **108** , 17886-17892.

38. D. M. Wood, A. Zunger, *J. Phys. A: Math Gen.* 1985, **18**, 1343-1359.

39. P. Pulay, *Chem. Phys. Lett.* 1980, **73**, 393-398.

40. M. R. Hartman, J.R. Rush, T.J. Udovic, R.C. Brownman and S.J. Hwang, J. *Solid State Chem.* 2007, **180**, 1298-1305.

41. W. Tang, E. Sanville and G. Henkelman, *J. Phys.: Condens. Matter* 2009, **21**, 084204.

42. G. Henkelman, B.P. Uberuaga, H. Jónsson, *J. Chem. Phys.* 2000, **113**, 9901-9905.

43. P. He, X. Wang, Y. Liu and L. Yi, Int. J. Hydrogen Energy 2012, **37**, 11984-11993.

44. M. Peter, J.M.F Camacho, S. Adamovski, L.K. Ono, K.H. Dostert, C.P. O'Brien, B. R. Cuenya, S. Schauermann and H. J. Freund, Angew. Chem. Int. Ed. 2013, 52, 1-6.

45. Y. Le Page, P. Saxe, *Phys. Rev. B* 2002, **65**, 104104-104128.

46. X. Wu, D. Vanderbilt, D. R. Hamann *Phys. Rev. B* 2005, **72**, 035105-035118.

47. K. Baldridge and A. Klamt, *J. Chem. Phys.* 1997, **106**, 6622-6633.

48. J. R. Pliego and J.M. Riveros, *J. Phys. Chem.*, 2000, **104**, 5155-5160.

Table 1: Geometry of Os nanoparticles where d, E_c, a_{NP}, $\boldsymbol{n}$, M are the diameter, cohesive energy, Os-Os distance, number of shells and magnetic moment, respectively.

No. of Atoms	d (~nm)	E_c (eV)	a_{NP} (Å)	$\boldsymbol{n}$	$M(\mu_B)$
57	1.00	8.63	2.63	2	0
89	1.50	8.90	2.65	4	0
214	2.00	9.30	2.68	6	0
Bulk	--	10.42	2.75	--	0

Table 2: Borohydride adsorption properties on Os (0001). Asterisk (*) indicates an adsorbed state. B, H1, H2 , H3 , H4 are boron and hydrogen atoms as labeled in Figure 3(b). The texts in bold form give the most stable adsorption geometry and those in italized form give the next most stable adsorption. Values in parenthesis give the dissociated B and H distances. Superscript *hl-t* in the second column represents relaxation to this most stable site.

Initial Configuration	Binding Energy, (E_b) eV	Final Structure	B-H1 distance (Å)	B-H2,3,4 distances (Å)
b-b	-4.87	BH_4*	1.21	1.43
b-h1	$-4.96^{h1\text{-}t}$	BH_4*	1.22	1.44-1.45
b-t	*-4.90*	*BH_3* + H**	*1.21*	*1.42-1.43 (2.80)*
b1-b	-3.61	BH* + 3H*	1.20	(1.81)
h1-t	**-4.96**	**BH_4***	**1.22**	**1.44-1.45**
h2-b	-3.17	BH_4*	1.20	1.41
h2-t	-4.87	BH_4*	1.22	1.43
t-b	-2.76	BH_4*	1.20	1.44-1.46
t-h1	-2.83	BH* + 3H*	1.19	(2.21)

Table 3: Borohydride adsorption properties on Os $(10\bar{1}0)$. Asterisk (*) indicates an adsorbed state. B, H1, H2, H3, H4 are boron and hydrogen atoms as shown in Figure 4(b). The texts in bold form give the most stable adsorption geometry and those in italized form give the next most stable adsorption. Values in parenthesis give the dissociated B and H distances.

Initial Configuration	Binding Energy, (E_b) eV	Final Structure	B-H_1 distance (Å)	B-H2,3,4 distances (Å)
b2-h1	*-5.38*	*BH* + 3H**	*1.20*	*(2.62-2.76)*
b2-t	**-5.64**	**BH_2* + 2H***	**1.21**	**1.42 (2.99)**
h2-t	-4.74	BH_4*	1.21	1.52-1.54
b1-h1	-4.10	BH_4*	1.20	1.38-1.39
b1-t	-4.74	BH* + 3H*	1.20	(2.02-2.72)
h1-b1	-4.67	BH_3* + H*	1.21	1.39-1.40 (3.17)
h1-h1	-5.24	BH_3* + H*	1.21	1.44 (3.37)
t-b1	-4.74	BH* + 3H*	1.20	(2.00-2.70)
t-h1	-3.58	BH_4*	1.20	1.63

Table 4: Borohydride adsorption properties on Os($1\bar{1}00$). Asterisk (*) indicates an adsorbed state. B, H1, H2 . H3 , H4 are the boron and hydrogen atoms as shown in Figure 5(b). The texts in bold form give the most stable adsorption geometry and those in italized form give the next most stable adsorption. Values in parenthesis give the dissociated B and H distances. Superscript *h-h* in the second column represents relaxation to this most stable site.

Initial Configuration	Binding Energy, (E_b) eV	Final Structure	B-H$_1$ distance (Å)	B-H2,3,4 distances (Å)
b2-h	-5.08	$\mathrm{BH_4}$*	1.20	1.33-1.34
b2-t	-5.13	$\mathrm{BH_4}$*	1.21	1.34-1.42
b1-h	$-5.41^{h\text{-}h}$	$\mathrm{BH_3}$* + H*	1.22	1.47-1.50 (2.83)
b1-t	-4.32	$\mathrm{BH_4}$*	1.20	1.34-1.42
h-b1	**-6.72**	**BH* + 3H***	**1.23**	**(3.31-3.35)**
h-h	*-5.41*	*BH_3* + H**	*1.22*	*1.47-1.50 (2.83)*
t-b1	-4.53	$\mathrm{BH_4}$*	1.19	1.32–1.67
t-h	-4.39	$\mathrm{BH_4}$*	1.19	1.30-1.43

Table 5: Adsorption of borohydride on Os-214 on different binding sites: (a)-(h) labeled based on the initial configuration depicted in Figure 6. The data in italized form, bold form and underscored describe the most stable adsorption on (0001), $(10\bar{1}0)$ and $(1\bar{1}00)$, respectively .

Plane	Site	Binding Energy, (E_b) eV	Final Structure	B-H$_1$ distance (Å)	B-H$_{2,3,4}$ distances (Å)
(0001)	(a)	-5.05	$\mathrm{BH_4*}$	1.22	1.46-1.47
	(b)	*-5.33*	*$\mathrm{BH_4*}$*	*1.22*	*1.38-1.44*
	(c)	-5.15	$\mathrm{BH_4*}$	1.22	1.39-1.42
$(10\bar{1}0)$	**(d)**	**-5.71**	**$\mathrm{BH_2* + 2H*}$**	**1.20**	**1.43(2.85-3.09)**
	(e)	-5.41	$\mathrm{BH_4*}$	1.22	1.43-1.49
	(f)	-5.66	$\mathrm{BH_3* + H*}$	1.21	1.42(2.99)
$(1\bar{1}00)$	(g)	-5.39	$\mathrm{BH* + 3H*}$	1.32	(2.46-4.19)
	(h)	-5.61	$\mathrm{BH_2* + 2H}$	1.21	1.59(2.91-2.94)

Table 6: Adsorption data for borohydride on (0001) plane of Os NP. The geometry and the sizes of the Os-NP correspond to the models shown in Figure 7.

Os NP	Binding Energy, (E_b) eV	Final Structure	B-H_1 distance (Å)	B-$H_{2,3,4}$ distances (Å)
Os-57	-4.79	BH_4*	1.22	1.40-1.42
Os-89	-4.85	BH_4*	1.22	1.41-1.46
Os-214	-5.33	BH_4*	1.22	1.38-1.44

Table 7: Oxidative adsorption calculation parameters: ground state energy (E_{DFT}), zero-point vibrational energy (E_{ZPVE}) and entropic term ($S_{vib}T$) for surface bound species, BH_4^* and H_2O^* on Os slab and Os-NP. The superscript letter correspond to the most stable configuration of the adsorbate on the NP as indicated in Figure 6.

	Os Surface (0001)		Os Nanoparticle (Os-214) (0001)[b]	
	BH_4^*	H_2O^*	BH_4^*	H_2O^*
E_{DFT}	-405.415	-397.440	-2191.040	-2183.525
E_{ZPVE}	0.954	0.641	0.952	0.644
$S_{vib}T$	0.075	0.191	0.082	0.184

Table 8: Geometry of Os-NP at 300K. a_{ave}, $b_{ave}$and c_{ave} are the average Os-Os edge distances and angles as shown in Figure 9. The corresponding distances and angles of Os-NP at 0K are shown in the parenthesis.

Os NP	a_{ave}	b_{ave}	$\angle c_{ave}$
Os-57	2.60 (2.64)	2.94 (2.66)	168.5° (180.0°)
Os-89	2.68 (2.67)	2.81 (2.68)	168.8°(180.0°)
Os-214	2.71 (2.69)	2.71 (2.69)	172.4°(180.0°)

Figure Captions:

Figure 1: Top and side views of the structure of the Os metal slabs in (a) (0001), (b) $(10\bar{1}0)$ and (c) $(1\bar{1}00)$ facets. Relevant distances are given: **a, b**, **c** are the lateral distances (**a** is the lattice parameter, **b** is the longer Os-Os distance between parallel rows of $(10\bar{1}0)$ and $(1\bar{1}00)$ and **c** is the distance between surface and subsurface atoms) and $d_{1\text{-}2}$, $d_{2\text{-}3}$ are the interlayer distances. Atoms on the surface and subsurfaces are labeled as 1 and 2 (or 3), respectively.

Figure 2: Os nanoparticles of sizes (a) ~1.0nm, (b) ~1.5nm and (c) ~2.0nm labeled as Os-57, Os-89 and Os-214, respectively. a_{NP} is the next neighboring distance. Some of the atoms belonging to the $(10\bar{1}0)$ and $(1\bar{1}00)$ planes are indicated by dashed lines in (c).

Figure 3: (a) Initial adsorption configuration of borohydride on Os (0001) and potential energy scanning scheme use to locate most preferred borohydride adsorption on metal surface. The adsorption sites are indicated as bridge (*b*), hollow (*h1*, *h2*) and top (*t*). The B and H atoms are labeled accordingly. (b) Final structure of the adsorbed specie.

Lateral Os-Os distances at the binding site, **a** and near the binding site, **a’** and other relevant distances ($d_{1\text{-}2}$, $d_{2\text{-}3}$) are given. The isolated gas phase borohydride molecule is shown in the inset figure.

Figure 4: (a). Initial adsorption configuration of borohydride on Os $(10\bar{1}0)$. The adsorption sites are shown as bridge (*b1, b2*), hollow (*h1*, *h2*) and top (*t*). *h2* is the hollow located at the center of the triangle drawn whose one vertex is a subsurface atom. (b) Final structure of the adsorbed specie. Lateral Os-Os distances at the binding site (**a, b, c**) and near the binding site (**a’**, **b’**, **c’**) and other relevant distances ($d_{1\text{-}2}$, $d_{2\text{-}3}$) are given. The B and H atoms are labeled accordingly.

Figure 5: (a). Initial adsorption configuration of borohydride on Os$(1\bar{1}00)$. The adsorption sites are shown as bridge (*b1, b2*), hollow (*h*) and top (*t*). (b) Final structure of the adsorbed specie. Lateral Os-Os distances at the binding site (**a, b, c**) and near the binding site (**a’**, **b’**, **c’**) and other relevant distances ($d_{1\text{-}2}$, $d_{2\text{-}3}$) are given. The B and H atoms are labeled accordingly.

Figure 6: Adsorption of borohydride on different planes of Os-214: (a)-(c) (0001), (d)-(f) $(10\bar{1}0)$ and (g)-(h) $(1\bar{1}00)$. The final structure of the adsorbed specie is depicted by the atom positions. The initial configuration is indicated by a triangle (dashed) where vertices represent the triangular conformation of hydrogen with the plane and the center describes the position of the B atom which are: (a) center, (b) edge-vertex site, (c) edge site, (d) bridge site 1, (e) hollow site , (f) bridge site 2, (g) bridge and (h) hollow site. In (d) and (h), the triangle and square (solid) show the conformation of the B with the Os-214.

Figure 7: Borohydride adsorption configuration and binding energy with respect to NP size of (a) Os-57, (b) Os-89 and (c) Os-214.

Figure 8: Plot of change in Gibbs free energy (ΔG_{ads}) with respect to electrode potential, U for (0001) facet of Os metal slab and Os NP. Solid and dashed lines represent initial oxidative adsorption on surface and NP, respectively.

Figure 9: Final structure of (a) Os-57, (b) Os-89 and (c) Os-214 at 300K. The local structures at each plane are indicated as a_{ave}, b_{ave} and $\angle c_{ave}$ which pertain to the average lateral distance involving one vertex and one edge atom of (0001) plane, lateral distance involving one vertex and one edge atom at $(10\bar{1}0)$ plane and angle between the Os-Os bonds at the edge of $(1\bar{1}00)$ plane, respectively.

Figure 1

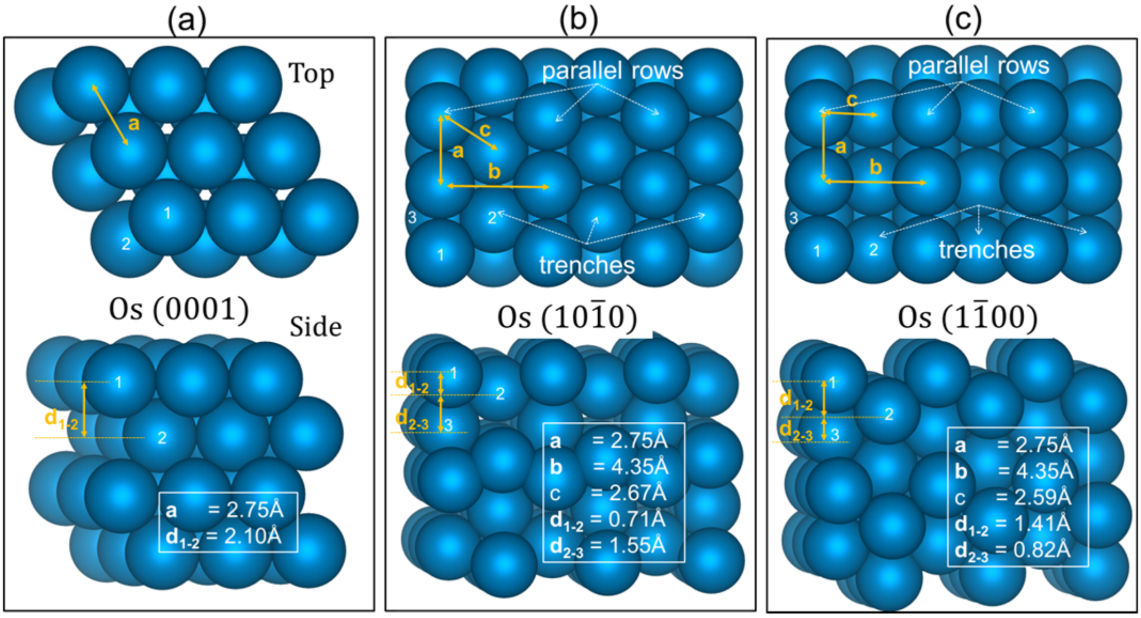
(a)
(b)
(c)
Top
Side
a
1
2
Os (0001)
d1-2
a = 2.75Å
d1-2 = 2.10Å
parallel rows
trenches
a
b
c
1
2
3
Os (10$\bar{1}$0)
d1-2
d2-3
a = 2.75Å
b = 4.35Å
c = 2.67Å
d1-2 = 0.71Å
d2-3 = 1.55Å
parallel rows
trenches
Os (1$\bar{1}$00)
a = 2.75Å
b = 4.35Å
c = 2.59Å
d1-2 = 1.41Å
d2-3 = 0.82Å

Figure 2

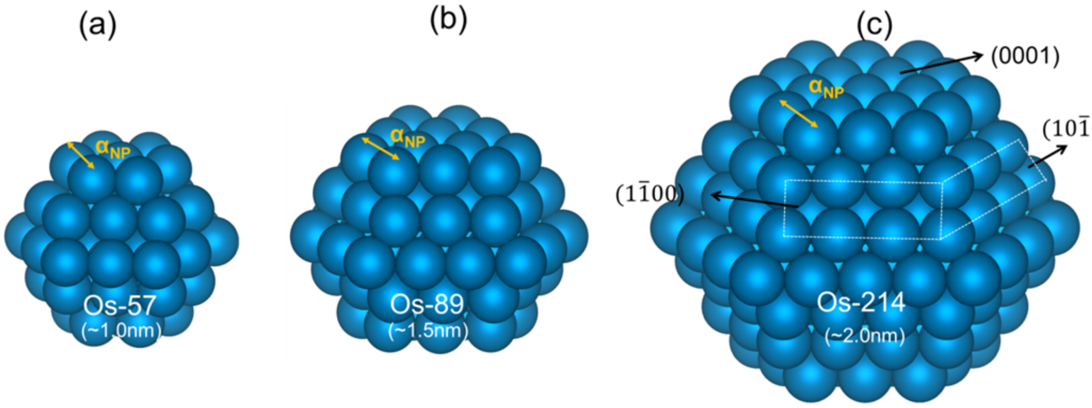
(a)
(b)
(c)
α_{NP}
α_{NP}
α_{NP}
Os-57
(~1.0nm)
Os-89
(~1.5nm)
Os-214
(~2.0nm)
(0001)
(10$\bar{1}$0)
(1$\bar{1}$00)

Figure 3

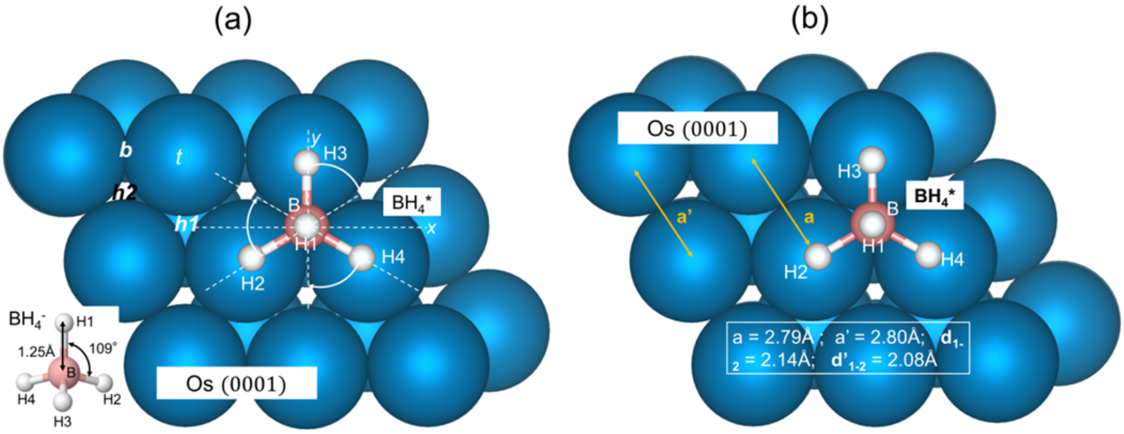
(a)
b
t
h2
h1
y
x
H3
B
H1
H2
H4
BH$_4$*
BH$_4^-$
H1
1.25Å
109°
B
H4
H2
H3
Os (0001)
(b)
Os (0001)
a'
a
H3
B
H1
H2
H4
BH$_4$*
a = 2.79Å ; a' = 2.80Å; d$_{1-2}$ = 2.14Å; d'$_{1-2}$ = 2.08Å

Figure 4

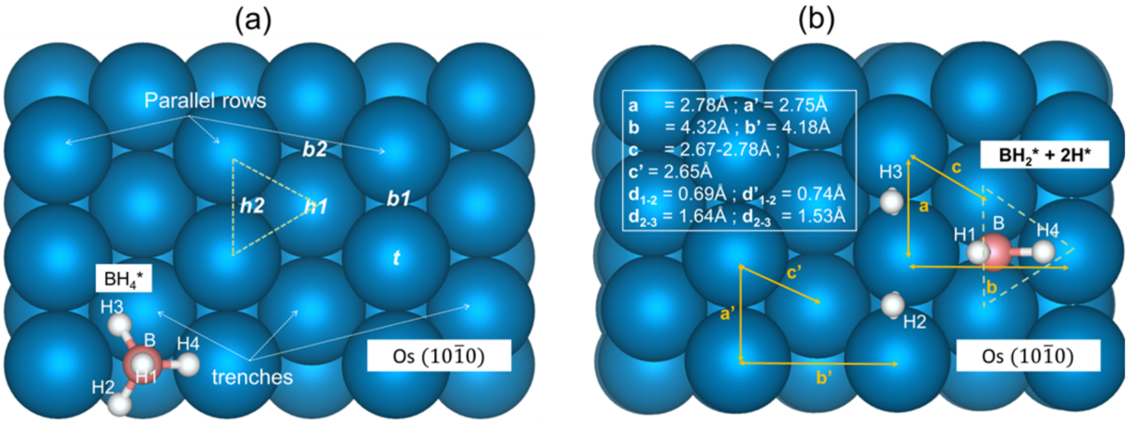
(a)
Parallel rows
b2
h2
h1
b1
t
BH$_4$*
H3
B
H4
H2
H1
trenches
Os (10$\bar{1}$0)
(b)
a = 2.78Å ; a' = 2.75Å
b = 4.32Å ; b' = 4.18Å
c = 2.67-2.78Å ;
c' = 2.65Å
d$_{1-2}$ = 0.69Å ; d'$_{1-2}$ = 0.74Å
d$_{2-3}$ = 1.64Å ; d$_{2-3}$ = 1.53Å
BH$_2$* + 2H*
H3
c
a
H1
B
H4
b
c'
a'
H2
b'
Os (10$\bar{1}$0)

Figure 5

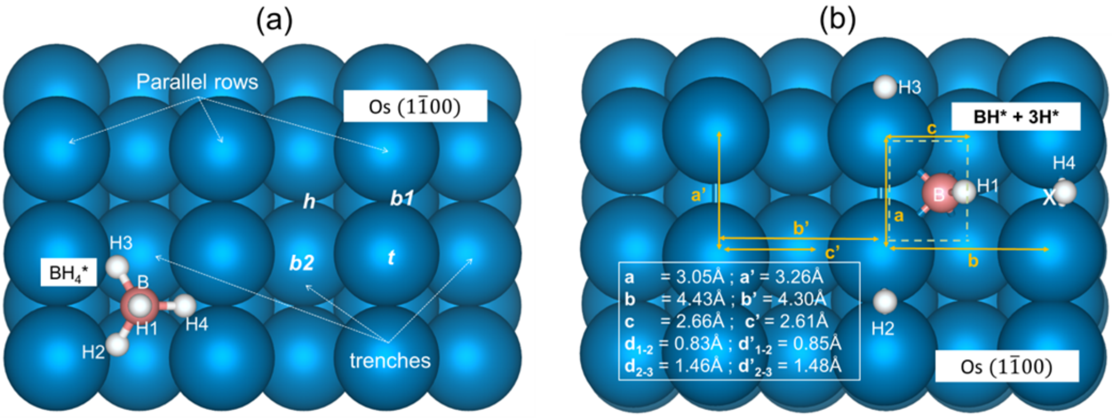
(a)
Parallel rows
Os $(1\bar{1}00)$
h
b1
b2
t
H3
BH_4^*
B
H1
H4
H2
trenches
(b)
H3
$BH^* + 3H^*$
c
H4
H1
B
X
a'
a
b'
c'
b
a = 3.05Å ; a' = 3.26Å
b = 4.43Å ; b' = 4.30Å
c = 2.66Å ; c' = 2.61Å
d_{1-2} = 0.83Å ; d'_{1-2} = 0.85Å
d_{2-3} = 1.46Å ; d'_{2-3} = 1.48Å
H2
Os $(1\bar{1}00)$

Figure 6

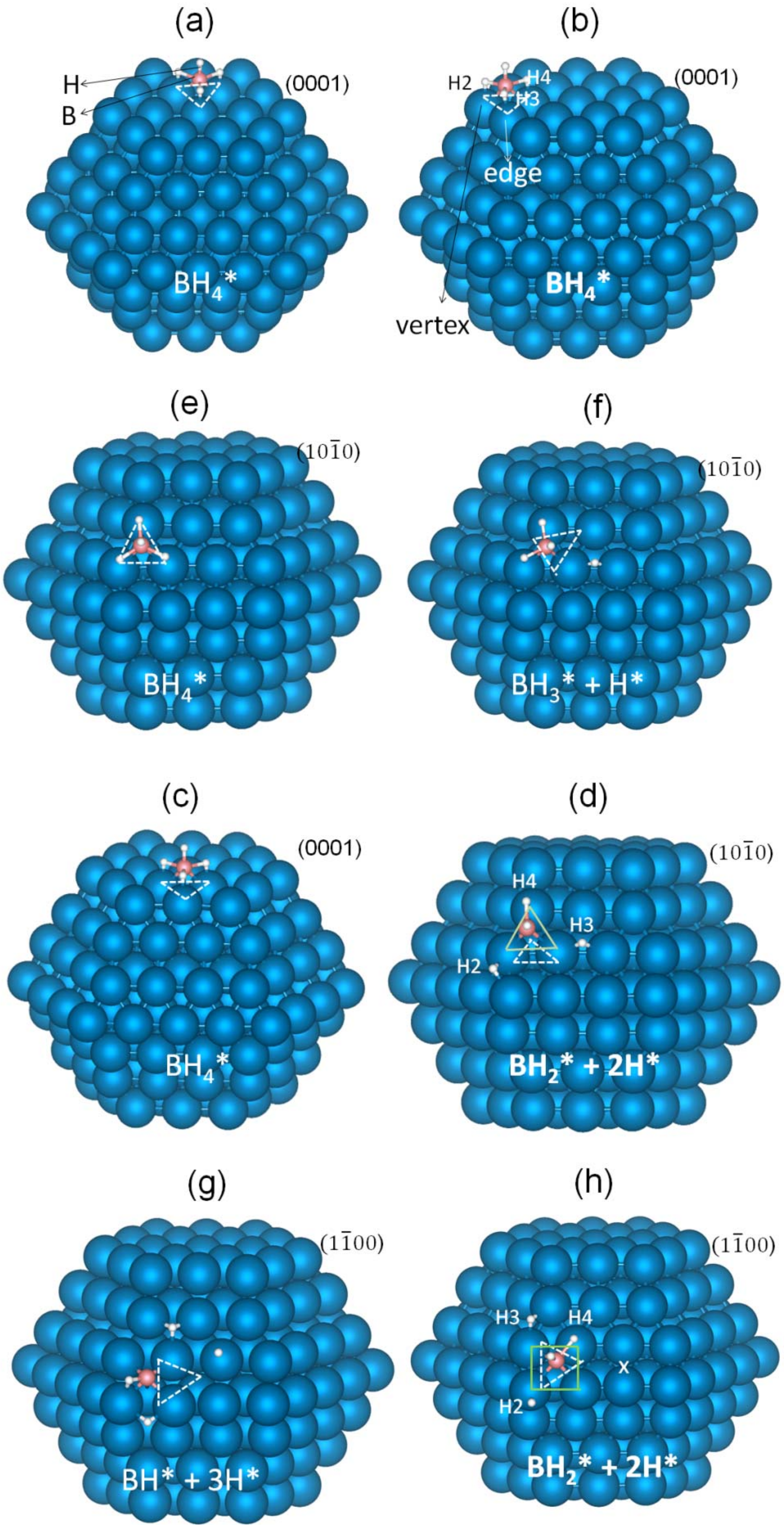
(a)
H
B
(0001)
BH_4*
(b)
H2
H4
H3
(0001)
edge
vertex
BH_4*
(e)
(10$\bar{1}$0)
BH_4*
(f)
(10$\bar{1}$0)
BH_3* + H*
(c)
(0001)
BH_4*
(d)
(10$\bar{1}$0)
H4
H3
H2
BH_2* + 2H*
(g)
(1$\bar{1}$00)
BH* + 3H*
(h)
(1$\bar{1}$00)
H3
H4
X
H2
BH_2* + 2H*

Figure 7

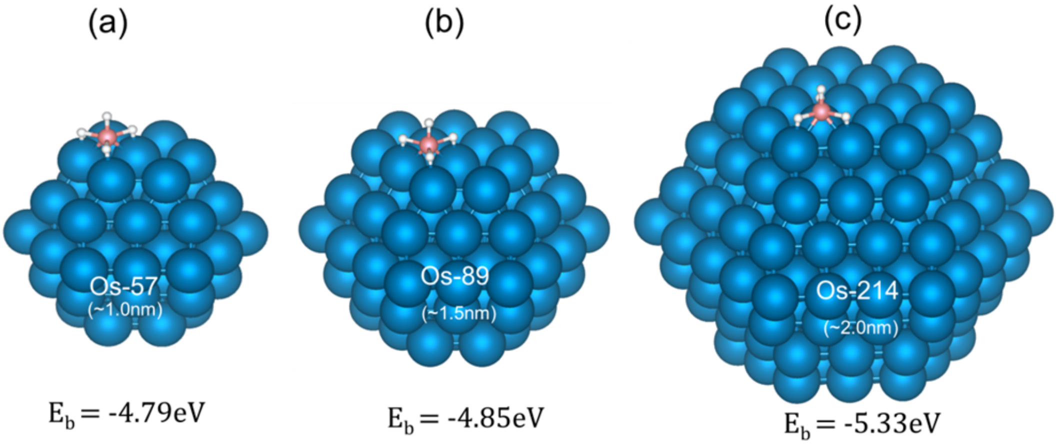

Figure 8

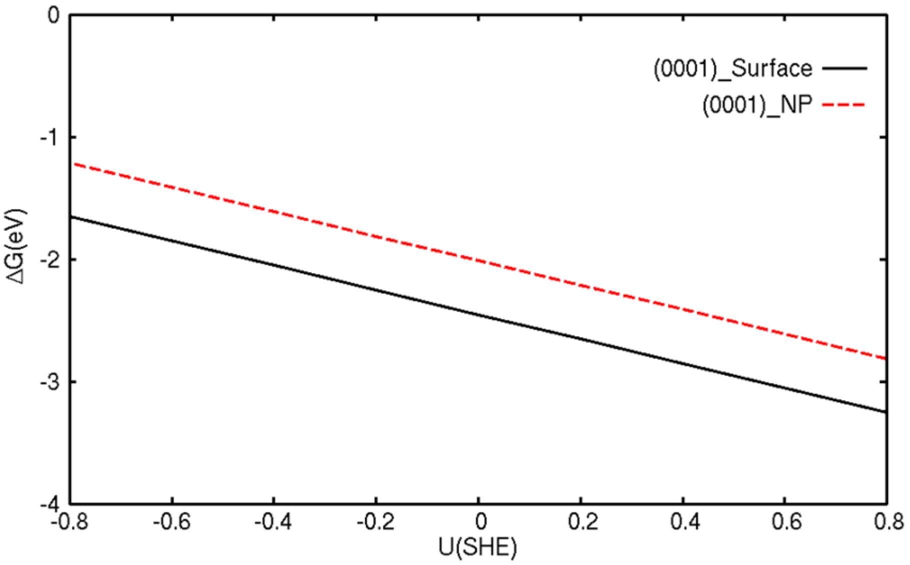

Figure 9